Research Square

Preprints are preliminary reports that have not undergone peer review.
They should not be considered conclusive, used to inform clinical practice,
or referenced by the media as validated information.

Real-time Crystallographic Capture of Fe–NO Bond Photodissociation in a Nonheme Iron Nitrosyl Complex

Jaeheung Cho

jaeheung@unist.ac.kr

Ulsan National Institute of Science and Technology https://orcid.org/0000-0002-2712-4295

Seungwon Sun

Ulsan National Institute of Science and Technology https://orcid.org/0000-0002-0874-6398

Sangho So

Korea Advanced Institute of Science and Technology

Dohyun Moon

Pohang Accelerator Laboratory https://orcid.org/0000-0002-6903-0270

Mu-Hyun Baik

Center for Catalytic Hydrocarbon Functionalizations, Institute for Basic Science (IBS)
https://orcid.org/0000-0002-8832-8187

Article

Keywords:

Posted Date: February 27th, 2026

DOI: https://doi.org/10.21203/rs.3.rs-6722143/v1

License: This work is licensed under a Creative Commons Attribution 4.0 International License.
Read Full License

Additional Declarations: There is **NO** Competing Interest.

Abstract

The interplay between nitric oxide ($NO^{\bullet}$) and iron (Fe) centers in metalloenzymes is central to many biological functions, with light-induced Fe – NO bond dissociation emerging as a key regulatory mechanism. Here, we present direct structural evidence for the stepwise dissociation of the Fe – NO bond in a crystalline nonheme iron nitrosyl complex, captured through in-situ photocrystallography under visible light. Marked Fe – NO bond elongation reveals real-time snapshots of excited-state fission at atomic resolution. Solution-phase studies confirm the generality of the observed photoreactivity. Multiconfigurational CASSCF calculations show the ground state as a resonance among Fe(I), Fe(II), and Fe(III) configurations, with a photoactive $Fe^{I}–NO^{+}$ contribution enabling $NO^{\bullet}$ release via metal-to-ligand charge transfer. Strategic placement of electron-withdrawing chlorides at the para-position of the pyridyl moiety further amplifies this character, promoting efficient $NO^{\bullet}$ dissociation. These findings delineate a detailed mechanism of Fe–NO bond cleavage and provide rare structural insights into transient photoinduced processes central to NO signaling and metalloenzyme function.

Introduction

Nitric oxide ($NO^{\bullet}$) is a key signaling molecule that regulates a variety of physiological and pathological processes in mammals, including vasodilatation, neurotransmission, and immune responses[1–7]. Endogenously, $NO^{\bullet}$ is produced through the enzymatic conversion of L-arginine to L-citrulline by nitric oxide synthase (NOS)[8,9]. Within physiological signaling pathways, $NO^{\bullet}$ receptors often contain heme Fe centers that can form Fe – NO adducts[3]. For instance, $NO^{\bullet}$ diffuses across the cell membrane to bind to the active site of soluble guanylate cyclase (sGC), leading to the production of cyclic guanosine monophosphate (cGMP), which facilitates vasorelaxation[10,11]. Beyond its physiological roles in mammals, $NO^{\bullet}$ also modulates catalysis in microbial systems. In particular, $NO^{\bullet}$ regulates the activity of Fe-containing nitrile hydratase (Fe-NHase), an enzyme that catalyzes the hydration of organic nitriles to their corresponding amides–an essential transformation in nitrile metabolism[12]. This regulation occurs via the reversible interaction of $NO^{\bullet}$ and the nonheme Fe center of Fe-NHase, in which light-induced cleavage of the Fe–NO bond and rebinding of $NO^{\bullet}$ to the Fe center modulates enzymatic activity[13,14].

In addition to its biological significance, the photoreactivity of nitrosyl complexes has garnered considerable attention in biomimetic and synthetic chemistry. The photolability of the metal–NO bond offers a promising strategy for the exogenous delivery of unstable $NO^{\bullet}$ with spatiotemporal precision, particularly for therapeutic applications. To investigate the light sensitivity of NO-containing metal complexes, a wide range of mononuclear nitrosyl species incorporating diverse metal centers and supporting ligands have been synthesized and characterized using various physicochemical techniques[15–31]. The photodissociation behavior in organic solvents has also been extensively studied[15,16,21]. Notably, model complexes of Fe-NHase featuring sulfinates (– SO_2) and thiolates (– S), which modulate $NO^{\bullet}$ binding affinity in metalloenzymes, exhibit high photolysis rates[23–26]. Analogous

nitrosyl complexes with Mn and Co centers have also demonstrated significant NO• release capabilities[15–19,30]. In contrast, Ru – NO complexes typically display lower photoreactivity, reflecting their greater thermodynamic stability compared to first-row transition metal analogues[32,33]. Recent theoretical studies attribute light-induced NO• dissociation to electronic excitation from bonding or non-bonding molecular orbitals to antibonding orbitals, typically mediated by metal-to-ligand charge transfer (MLCT) or ligand-to-metal charge transfer (LMCT) transitions[30,31,34–39].

Despite extensive research on photolabile nitrosyl complexes and their dissociation mechanisms, a precise understanding of the Fe – NO bonding remains elusive. This challenge arises from the highly covalent nature of the Fe – NO bond and the redox non-innocence of the NO• ligand[40,41]. Moreover, although numerous studies have investigated photolabile metal-nitrosyl species, none have directly captured the photodissociation process through experimentally resolved geometric changes–such as bond lengths and angles–at atomic resolution.

In this study, we report the first crystallographic observation of stepwise Fe–NO bond dissociation under visible light irradiation. Using in-situ single-crystal X-ray diffraction, we monitored the structural evolution of the iron nitrosyl complex, $[Fe(Cl–TBDAP)(NO)(H_2O)]^{2+}$ (**2**), in real time during photolysis. The data reveal a consistent elongation of the Fe – NO bond accompanied by a concurrent shortening of the N–O bond. These structural changes provide high-resolution insight into the excited state dynamics of the Fe–NO photodissociation and offers new perspective on the bonding within the Fe–N–O unit.

Results and discussion

Synthesis and characterization of 1 and 2

The Fe(II) precursor complex, $[Fe^{II}(Cl–TBDAP)(CH_3CN)(OTf)]^+$ (**1**) (Cl–TBDAP = *N*,*N*′-di-*tert*-butyl-2,11-diaza[3.3](2,6)-*p*-chloro-pyridinophane), was synthesized by reacting anhydrous $FeCl_2$ with one equivalent of the Cl–TBDAP ligand and two equivalents of AgOTf (Fig. 1a). Complex **1** was characterized by ultraviolet-visible (UV-vis) spectroscopy, electrospray ionization mass spectrometry (ESI-MS), and single crystal X-ray diffractometry (SC-XRD) (Supplementary Figs. S1–S3 and Tables S1–S2). Exposure of **1** to excess nitric oxide gas in acetone at − 40°C yielded a reddish-brown solution of **2** (Fig. 1a). The UV-vis spectrum of **2** displayed absorption bands at λ_{max} = 408 (ε = 1027 M^{-1} cm^{-1}), 515 (ε = 351 M^{-1} cm^{-1}), and 741 nm (ε = 138 M^{-1} cm^{-1}) (Fig. 1b)[31]. Complex **2** was stable at − 40°C in the absence of light, allowing for the growth of single crystals suitable for structural, spectroscopic, and photochemical studies. Cold-spray ionization mass spectrometry (CSI-MS) of **2** revealed prominent ion peaks at mass-to-charge ratio (*m/z*) of 282.0 and 654.9, consistent with the calculated values for $[Fe(Cl–TBDAP)(NO)(CH_3COCH_3)]^{2+}$ (*m/z* = 282.1) and $[Fe(Cl–TBDAP)(NO)(OTf)]^+$ (*m/z* = 655.1), respectively (Fig. 1c and Supplementary Fig. S5).

The single-crystal X-ray structure of **2** revealed a distorted octahedral coordination geometry, with four N atoms from the Cl–TBDAP ligand, a bound NO group, and a water molecule completing the coordination sphere (Fig. 1d). The Fe – NO and N – O bond lengths were determined to be 1.762(4) and 1.157(4) Å, respectively, with a bent Fe – N–O angle of 152.8(4)° (Supplementary Table S2)[42–44]. These values closely match those reported for the related complex $[Fe(TBDAP)(NO)(H_2O)]^{2+}$, (1.754 Å for Fe – NO; 1.153 Å for N – O; 152.9° for Fe – N–O)[31]. The attenuated total reflectance infrared (ATR-IR) spectrum of crystalline **2** exhibited an N – O stretching vibration band at 1766 cm^{-1}; consistent with the reported range of 1720–1800 cm^{-1} for high-spin $\{FeNO\}^7$ complexes and further supporting the assignment of a bound nitrosyl ligand as established by crystallography (Fig. 1b, inset and Supplementary Fig. S4)[31,42–47].

The X-band electron paramagnetic resonance (EPR) spectrum of **2** in frozen acetone at 100 K displayed *g* values of 3.71 and 1.99, consistent with an $S = 3/2$ spin state of **2** (Supplementary Fig. S6)[42–45]. This assignment is further supported by a low-temperature magnetic moment of 4.26 μ_B, determined by the ^1H NMR Evans method. Collectively, the characterization data obtained from SC-XRD, ATR-IR, EPR, and magnetic susceptibility are consistent with those of typical six-coordinate high-spin $\{FeNO\}^7$ complexes. Accordingly, **2** is best formulated as $[Fe(Cl–TBDAP)(NO)(H_2O)]^{2+}$, possessing a formal $Fe^{III}–NO^-$ ground state ($S = 3/2$), in which high-spin Fe^{III} ($S = 5/2$) and NO^- ($S = 1$) are antiferromagnetically coupled[31,42–47].

Photodissociation of 2 in solution

The light-induced Fe – NO bond dissociation in **2** was investigated under white light irradiation (λ_{irr} = 385–740 nm, 500 mW, xenon lamp) (Fig. 2a). The kinetics of photodissociation were monitored by following the decay of the absorption band at 515 nm. In the absence of light, the acetone solution of **2** was stable at − 40°C with no detectable spectral changes (Fig. 2b, inset, red). Upon irradiation, however, a rapid decrease in the 515 nm absorption band was observed (Fig. 2b, inset, black), indicative of Fe – NO bond cleavage. Notably, partial rebinding of $NO^•$ to the Fe center occurred when the xenon lamp was turned off. The Fe – NO dissociation followed first-order kinetics, with the observed rate constant (k_{obs}) increasing proportionally with light intensity (Supplementary Fig. S9)[16]. The enhanced photoreactivity of **2** is attributed to the electron-withdrawing Cl substituent on the TBDAP ligand. This substitution increases the population of the $Fe^{I}–NO^+$ configuration, facilitating the metal-to-ligand charge transfer (MLCT) absorption that promotes $NO^•$ release (*vide infra*)[31]. Consistent with this electronic effect, the redox potential of **2** is elevated relative to its parent complex $[Fe(TBDAP)(NO)(H_2O)]^{2+}$, resulting in a photodissociation rate that is 3.2 times higher (Supplementary Figs. S10 and S11).

Following photolysis, the final UV-vis spectrum of the solution exhibited an absorption profile similar to that of the Fe(II) precursor **1**, consistent with the loss of $NO^•$ and formation of a reduced Fe species (Supplementary Fig. S7). The presence of Fe(II) was further confirmed by ESI-MS measurements (Supplementary Fig. S8). To verify the release of free $NO^•$, the gas was captured using [Co(TPP)] (TPP =

5,10,15,20-tetraphenyl-21H,23H-porphine). After 30 minutes of light exposure, the characteristic UV-vis absorption bands of [Co(TPP)] at 410 and 528 nm shifted to 414 and 538 nm, respectively, indicating the formation of [Co(NO)(TPP)] (Supplementary Fig. S12)[26,27,30,31].

Photodissociation of 2 in solid

The photodissociation behavior of the Fe – NO bond in the solid state was investigated using single-crystal in-situ photocrystallography. Diffraction data were collected serially from a single crystal of **2**, with one dataset acquired every 130 seconds over a total irradiation period of 75 minutes under visible light. This time-resolved approach enabled the continuous monitoring of changes in the Fe – NO and N – O bond lengths (Supplementary Fig. S14 and Table S3). Upon irradiation, the Fe – NO bond length progressively increased from 1.762(4) to 1.805(10) Å, while the N – O bond length decreased from 1.157(4) to 1.103(9) Å. Concurrently, the Fe – N–O bond angle exhibited a slight bend, shifting from 152.8(4) to 150.9(10)°. The observed 0.054 Å shortening of the N – O bond is particularly notable and is comparable to the ~ 0.05 Å bond difference between free $NO^{\bullet}$ (1.15 Å) and NO^{-} (~ 1.20 Å), indicating a significant change in bonding character[3]. The time-dependent changes in Fe – NO elongation and N – O contraction displayed opposite trends with saturation behavior (Fig. 3b).

Despite the elongation of the Fe – NO bond to 1.805(10) Å, $NO^{\bullet}$ remained coordinated within the crystal lattice. This retention is likely due to steric confinement around the Fe – NO moiety. In the crystal structure, the NO ligand is surrounded by two triflate (OTf^{-}) counterions and one acetone molecule, positioned at an average distance of 3.22 Å. Additionally, another molecule of complex **2** is located above the NO ligand at a distance of 3.35 Å. A hydrogen-bonding network involving two OTf^{-} anions and two coordinated H_2O molecules further contributes to the rigidity of the lattice, as illustrated by the ORTEP and space-filling models (Supplementary Fig. S13). These steric and non-covalent interactions collectively hinder the complete dissociation and diffusion $NO^{\bullet}$ from the crystal matrix.

Changes in the N – O stretching frequency upon photodissociation were evaluated by ATR-IR spectroscopy. A pristine crystal of **2** and a photoactivated crystal irradiated for 60 minutes were compared. After light exposure, the N–O stretching band shifted from 1766 cm^{-1} to 1771 cm^{-1}, while the C – O stretching vibration of acetone at 1700 cm^{-1} remained unchanged (Fig. 3c). The 5 cm^{-1} blue shift in the N–O vibration correlates with the 0.054 Å decrease in the N–O bond length and is comparable to previous reports on nickel nitrosyl complexes, where a 0.04 Å contraction in N – O bond length led to a 6 cm^{-1} shift in stretching frequency (e.g., $PhB(^{Ad}Im)_3NiNO$: ν_{NO} = 1689 cm^{-1}, N–O: 1.183 Å; $HB(^{CF_3}mIm)_3NiNO$: ν_{NO} = 1695 cm^{-1}, N–O: 1.14 Å)[48].

Computational studies

To elucidate the electronic structure and the mechanism of $NO^{\bullet}$ release, complete active space self-consistent field (CASSCF) calculations were performed. In order to describe the bonding nature of the $\{FeNO\}^7$ unit accurately, an active space was selected that includes all electrons and orbitals associated with the Fe and NO moieties, as well as key ligand-based (See supporting information for details). The resulting CAS wavefunction was decomposed into five Fe d-orbitals and two NO-π* orbitals, as illustrated in Fig. 4. The projection of 5.49 electrons into the Fe d-dominated molecular orbitals indicates that the Fe center is best described as Fe^{III} in a d^5 configuration. Simultaneously, 0.88 and 0.80 electrons were found in the NO-π_y* and NO-π_z* orbitals, respectively, supporting an assignment of the NO ligand as anionic (NO^-). The ground state is predominantly described by the configuration (Fe-$d_{x^2-y^2}$)$^{\uparrow}$(Fe-d_{xy})$^{\uparrow}$(Fe-d_{z^2})$^{\uparrow}$(Fe-d_{yz})$^{\uparrow}$(Fe-d_{xz})$^{\uparrow}$(NO-π*$_y$)$^{\downarrow}$(NO-π*$_z$)$^{\downarrow}$, which contributes approximately 45% to the total wavefunction (Supplementary Table S5). This configuration corresponds to a high-spin Fe^{III} center (S = 5/2) antiferromagnetically coupled to a triplet NO^- moiety (S = 1), consistent with an overall S = 3/2 ground state and in agreement with experimental characterization described above. These results support the Fe^{III}–NO^- formulation of complex **2**[49].

To further investigate the excited-state behavior of **2**, state-averaged CASSCF calculations were conducted. In line with previous work[31], the Fe^{I}–NO^+ resonance form, which is only a minor contributor to the ground state, was found to be the key photoactive configuration. The lowest excited states, including Q_1, predominantly exhibit Fe^{II}–$NO^{\bullet}$ character and arise via a MLCT transition from Fe^{I}–NO^+. These transitions involve electron promotion from the Fe d-dominated Fe–NO bonding orbitals to the NO-π* dominated Fe–NO antibonding orbitals, thereby weakening the Fe–NO bond and promoting $NO^{\bullet}$ release (Supplementary Table S6 and Fig. S17).

The effect of substituent electrics was also explored. In the parent complex $[Fe(TBDAP)(NO)(H_2O)]^{2+}$, 0.91 and 0.80 electrons were localized in the NO-π_y* and NO-π_z* orbitals, respectively. By contrast, in complex **2**, para-chloride substitution reduces the electron density on these orbitals and increases the Fe^{I}–NO^+ character (Supplementary Fig. S18), thereby accelerating $NO^{\bullet}$ release. These findings strongly support the conclusion that $NO^{\bullet}$ dissociation proceeds via an MLCT originating from a minor Fe^{I}–NO^+ ground state resonance contributor.

Finally, geometry optimization of the lowest-lying excited state (Q_1) was performed at the CASSCF level. During this process, the Fe–NO complex was observed to dissociate into two fragments: free $NO^{\bullet}$ and the remaining Fe complex. The two products stabilized separately, and the calculation ultimately failed to converge to a single wavefunction encompassing both fragments. This result provides compelling computational evidence that photoexcitation leads to complete and spontaneous $NO^{\bullet}$ release and physical separation from the Fe center (Fig. 5).

Conclusions

In this study, we conducted a comprehensive investigation of the stepwise photodissociation of Fe − NO bond in the crystalline mononuclear nonheme high-spin $\{FeNO\}^7$ complex, $[Fe(Cl{-}TBDAP)(NO)(H_2O)]^{2+}$ (**2**), using in-situ single-crystal photocrystallography. Sequential X-ray data collection under visible light irradiation enabled real-time monitoring of structural changes within the crystal lattice, providing direct experimental evidence of bond dissociation dynamics. The photoreaction was characterized by progressive elongation of the Fe − NO bond and a simultaneous contraction of the N − O bond, revealing specific geometric signatures of excited-state reactivity. The correlation between bond length changes and irradiation time underscore the photolabile nature of **2** in solid state.

Importantly, the influence of the para-substituted Cl group on the photochemical properties of **2** was elucidated. As electron-withdrawing substituent, the Cl group decreases electron density in the NO-π* orbitals, thereby enhancing the contribution of the $Fe^{I}–NO^{+}$ resonance form. The adjustment in electronic structure increases the susceptibility of the Fe − NO bond to photodissociation in solution, facilitating $NO^{\bullet}$ release via a metal-to-ligand charge transfer process.

State-averaged CASSCF calculations complemented the experimental findings by providing detailed insights into the electronic structure and excited-state behavior of the Fe − NO unit. These results confirm that $NO^{\bullet}$ release proceeds through an MLCT transition from the minor $Fe^{I}–NO^{+}$ component of the ground-state wavefunction. Together, the integration of high-resolution structural data and multiconfigurational electronic structure analysis offers a molecular-level understanding of Fe–NO photoreactivity. This work advances the fundamental knowledge of Fe–NO bonding and photodissociation, with broader implications for biological $NO^{\bullet}$ regulation and the rational design of synthetic nitrosyl complexes for light-controlled $NO^{\bullet}$ delivery.

Declarations

Data availability

The data supporting the findings of this study are available within the paper and its Supplementary Information. Crystallographic data for the **1**-(OTf), **2**-$(OTf)_2$·CH_3COCH, and photocrystallography have been deposited at the Cambridge Crystallographic Data Centre (CCDC) under deposition numbers CCDC 2452720, CCDC 2452919, and CCDC 2452920–2452969, respectively. These data can be obtained free of charge from the CCDC (http://www.ccdc.cam.ac.uk/data_request/cif). Source data are provided with this paper.

Acknowledgements

The research was supported by the National Research Foundation funded by the Ministry of Science, ICT and Future Planning (RS-2024-00333606) and the Ministry of Health and Welfare (RS-2023-00217242) of Korea. We thank the Institute for Basic Science (IBS-R10-A1) in Korea for financial support. This material is based upon work supported by the National Science Foundation under Grant No. 1651686. The

synchrotron photocrystallography was supported by Basic Science Research Program through the National Research Foundation of Korea (NRF) funded by the Ministry of Education, Science and Technology (NRF-2021R1A2C1003080).

Author contributions

S. Sun, S. So, M.-H. B., and J. C. conceived and designed the experiments. S. Sun carried out synthesis and experimental work. D. M. conducted the SC-XRD experiment. S. So performed the computational calculations. All authors contributed to data analysis. S. Sun, S. So, M.-H. B., and J. C. co-wrote the paper.

Competing interests

The authors declare no competing interests.

References

1. Culotta E, Koshland DE (1992) NO news is good news. Science 258:1862–1865
2. Toledo JC Jr, Augusto O (2012) Connecting the chemical and biological properties of nitric oxide. Chem Res Toxicol 25:975–989
3. Lehnert N, Kim E, Dong HT, Harland JB, Hunt AP, Manickas EC, Oakley KM, Pham J, Reed GC, Alfaro VS (2021) The biologically relevant coordination chemistry of iron and nitric oxide: electronic structure and reactivity. Chem Rev 121:14682–14905
4. Farah C, Michel LYM, Balligand J-L (2018) Nitric oxide signalling in cardiovascular health and disease. Nat Rev Cardiol 15:292–316
5. Palmer RMJ, Ferrige AG, Moncada S (1987) Nitric oxide release accounts for the biological activity of endothelium-derived relaxing factor. Nature 327:524–526
6. Snyder SH (1992) Nitric oxide: first in a new class of neurotransmitters. Science 257:494–496
7. Wei XQ, Charles IG, Smith A, Ure J, Feng GJ, Huang FP, Xu D, Muller W, Moncada S, Liew F (1995) Y. Altered immune responses in mice lacking inducible nitric oxide synthase. Nature 375:408–411
8. Kwon NS, Nathan CF, Gilker C, Griffith OW, Matthews DE, Stuehr DJ (1990) L-citrulline production from L-arginine by macrophage nitric oxide synthase. the ureido oxygen derives from dioxygen. J Biol Chem 265:13442–13445
9. Rosen GM, Tsai P, Pou S (2002) Mechanism of free-radical generation by nitric oxide synthase. Chem Rev 102:1191–1200
10. Liu R, Kang Y, Chen L (2021) Activation mechanism of human soluble guanylate cyclase by stimulators and activators. Nat Commun 12:5492
11. Kang Y, Liu R, Wu J-X, Chen L (2019) Structural insights into the mechanism of human soluble guanylate cyclase. Nature 574:206–210
12. Endo I, Nojiri M, Tsujimura M, Nakasako M, Nagashima S, Yohda M, Odaka M (2001) Fe-type nitrile hydratase. J Inorg Biochem 83:247–253

13. Odaka M, Fujii K, Hoshino M, Noguchi T, Tsujimura M, Nagashima S, Yohda M, Nagamune T, Inoue Y, Endo I (1997) Activity regulation of photoreactive nitrile hydratase by nitric oxide. J Am Chem Soc 119:3785–3791
14. Endo I, Odaka M, Yohda M (1999) An enzyme controlled by light: the molecular mechanism of photoreactivity in nitrile hydratase. Trends Biotechnol 17:244–248
15. Ghosh K, Eroy-Reveles AA, Avila B, Holman TR, Olmstead MM, Mascharak PK (2004) Reactions of NO with Mn(II) and Mn(III) centers coordinated to carboxamido nitrogen: synthesis of a manganese nitrosyl with photolabile NO. Inorg Chem 43:2988–2997
16. Eroy-Reveles AA, Leung Y, Beavers CM, Olmstead MM, Mascharak PK (2008) Near-infrared light activated release of nitric oxide from designed photoactive manganese nitrosyls: strategy, design, and potential as NO donors. J Am Chem Soc 130:4447–4458
17. Hoffman-Luca CG, Eroy-Reveles AA, Alvarenga J, Mascharak PK (2009) Syntheses, structures, and photochemistry of manganese nitrosyls derived from designed schiff base ligands: potential NO donors that can be activated by near-infrared light. Inorg Chem 48:9104–9111
18. Hitomi Y, Iwamoto Y, Kodera M (2014) Electronic tuning of nitric oxide release from manganese nitrosyl complexes by visible light irradiation: enhancement of nitric oxide release efficiency by the nitro-substituted quinoline ligand. Dalton Trans 43:2161–2167
19. Iwamoto Y, Kodera M, Hitomi Y (2015) Uncaging a catalytic hydrogen peroxide generator through the photo-induced release of nitric oxide from a $\{MnNO\}^6$ complex. Chem Commun 51:9539–9542
20. Patra AK, Afshar R, Olmstead MM, Mascharak PK (2002) The first non-heme iron(III) complex with a ligated carboxamido group that exhibits photolability of a bound NO ligand. Angew Chem Int Ed 41:2512–2515
21. Patra AK, Rowland JM, Marlin DS, Bill E, Olmstead MM, Mascharak PK (2003) Iron nitrosyls of a pentadentate ligand containing a single carboxamide group: syntheses, structures, electronic properties, and photolability of NO. Inorg Chem 42:6812–6823
22. Afshar RK, Patra AK, Olmstead MM, Mascharak PK (2004) Syntheses, structures, and reactivities of $\{Fe – NO\}^6$ nitrosyls derived from polypyridine-carboxamide ligands: photoactive NO-donors and reagents for S-nitrosylation of alkyl thiols. Inorg Chem 43:5736–5743
23. Szaciłowski K, Chmura A, Stasicka Z (2005) Interplay between iron complexes, nitric oxide and sulfur ligands: structure, (photo)reactivity and biological importance. Coord Chem Rev 249:2408–2436
24. Schweitzer D, Ellison JJ, Shoner SC, Lovell S, Kovacs JA (1998) A synthetic model for the NO-inactivated form of nitrile hydratase. J Am Chem Soc 120:10996–10997
25. Rose MJ, Betterley NM, Mascharak PK (2009) Thiolate S-oxygenation controls nitric oxide (NO) photolability of a synthetic iron nitrile hydratase (Fe-NHase) model derived from mixed carboxamide/thiolate ligand. J Am Chem Soc 131:8340–8341
26. Dey A, Confer AM, Vilbert AC, Moënne-Loccoz P, Lancaster KM, Goldberg (2018) D. P. A nonheme sulfur-ligated $\{FeNO\}^6$ complex and comparison with redox-interconvertible $\{FeNO\}^7$ and $\{FeNO\}^8$

analogues. Angew Chem Int Ed 57:13465–13469

27. McQuilken AC, Matsumura H, Dürr M, Confer AM, Sheckelton JP, Siegler MA, McQueen TM, Ivanović-Burmazović I, Moënne-Loccoz P (2016) Goldberg, D. P. Photoinitiated reactivity of a thiolate-ligated, spin-crossover nonheme $\{FeNO\}^7$ complex with dioxygen. J Am Chem Soc 138:3107–3117
28. McQuilken AC, Ha Y, Sutherlin KD, Siegler MA, Hodgson KO, Hedman B, Solomon EI, Jameson GN, Goldberg DP (2013) Preparation of non-heme $\{FeNO\}^7$ models of cysteine dioxygenase: sulfur versus nitrogen ligation and photorelease of nitric oxide. J Am Chem Soc 135:14024–14027
29. Chiang C-K, Chu K-T, Lin C-C, Xie S-R, Liu Y-C, Demeshko S, Lee G-H, Meyer F, Tsai M-L, Chiang M-H, Lee C-M (2020) Photoinduced NO and HNO production from mononuclear $\{FeNO\}^6$ complex bearing a pendant thiol. J Am Chem Soc 142:8649–8661
30. Shin S, Choe J, Park Y, Jeong D, Song H, You Y, Seo D, Cho J (2019) Artificial control of cell signaling using a photocleavable cobalt(III)–nitrosyl complex. Angew Chem Int Ed 58:10126–10131
31. Choe J, Kim SJ, Kim J-H, Baik M-H, Lee J, Cho J (2023) Photodynamic treatment of acute vascular occlusion by using an iron–nitrosyl complex. Chem 9:1309–1317
32. Fry NL, Heilman BJ, Mascharak PK (2011) Dye-tethered ruthenium nitrosyls containing planar dicarboxamide tetradentate N4 ligands: effects of in-plane ligand twist on NO photolability. Inorg Chem 50:317–324
33. Rose MJ, Mascharak PK (2008) Photoactive ruthenium nitrosyls: effects of light and potential application as NO donors. Coord Chem Rev 252:2093–2114
34. Greene SN, Richards NGJ (2004) Theoretical investigations of the electronic structure and spectroscopy of mononuclear, non-heme $\{Fe – NO\}^6$ complexes. Inorg Chem 43:7030–7041
35. Fry NL, Zhao XP, Mascharak PK (2011) Density functional theory studies on a designed photoactive $\{FeNO\}^6$ nitrosyl and the corresponding photoinactive $\{FeNO\}^7$ species: insight into the origin of NO photolability. Inorg Chim Acta 367:194–198
36. Merkle AC, Fry NL, Mascharak PK, Lehnert N (2011) Mechanism of NO photodissociation in photolabile manganese–NO complexes with pentadentate N5 ligands. Inorg Chem 50:12192–12203
37. Fry NL, Mascharak PK (2012) Photolability of NO in designed metal nitrosyls with carboxamido-N donors: a theoretical attempt to unravel the mechanism. Dalton Trans 41:4726–4735
38. Zheng W, Wu S, Zhao S, Geng Y, Jin J, Su Z, Fu Q (2012) Carbonyl amine/schiff base ligands in manganese complexes: theoretical study on the mechanism, capability of NO release. Inorg Chem 51:3972–3980
39. Freitag L, González L (2014) Theoretical spectroscopy and photodynamics of a ruthenium nitrosyl complex. Inorg Chem 53:6415–6426
40. Lewandowska H (2013) Nitrosyl complexes in inorganic chemistry, biochemistry and medicine I. Struct Bond 115–165. 10.1007/430_2013_109
41. Sun S, Choe J, Cho J (2024) Photo-triggered NO release of nitrosyl complexes bearing first-row transition metals and therapeutic applications. Chem Sci 15:20155–20170

42. Berto TC, Speelman AL, Zheng S, Lehnert N (2013) Mono- and dinuclear non-heme iron–nitrosyl complexes: models for key intermediates in bacterial nitric oxide reductases. Coord Chem Rev 257:244–259
43. Li J, Banerjee A, Pawlak PL, Brennessel WW, Chavez FA (2014) Highest recorded N–O stretching frequency for 6-coordinate {Fe-NO}^{7} complexes: an iron nitrosyl model for His_3 active sites. Inorg Chem 53:5414–5416
44. Berto TC, Hoffman MB, Murata Y, Landenberger KB, Alp EE, Zhao J, Lehnert N (2011) Structural and electronic characterization of non-heme Fe(II)–nitrosyls as biomimetic models of the Fe_B center of bacterial nitric oxide reductase. J Am Chem Soc 133:16714–16717
45. Dey A, Gordon JB, Albert T, Sabuncu S, Siegler MA, MacMillan SN, Lancaster KM, Moënne-Loccoz P, Goldberg D (2021) P. A nonheme mononuclear {FeNO}^{7} complex that produces N_2O in the absence of an exogenous reductant. Angew Chem Int Ed 60:21558–21564
46. Dong HT, Speelman AL, Kozemchak CE, Sil D, Krebs C, Lehnert N (2019) The $Fe_2(NO)_2$ diamond core: a unique structural motif in non-heme iron–NO chemistry. Angew Chem Int Ed 58:17695–17699
47. Dong HT, Camarena S, Sil D, Lengel MO, Zhao J, Hu MY, Alp EE, Krebs C, Lehnert N (2022) What is the right level of activation of a high-spin {FeNO}^{7} complex to enable direct N–N coupling? mechanistic insight into flavodiiron NO reductases. J Am Chem Soc 144:16395–16409
48. Scott JS, Schneider JE, Tewelde EG, Gardner JG, Anferov SW, Filatov AS, Anderson JS (2023) Combining donor strength and oxidative stability in scorpionates: a strongly donating fluorinated mesoionic tris(imidazol-5-ylidene)borate ligand. Inorg Chem 62:21224–21232
49. Radoń M, Broclawik E, Pierloot K (2010) Electronic structure of selected {FeNO}. complexes heme non-heme architectures: density Funct multireference ab initio study J Phys Chem B 114:1518–1528

Figures

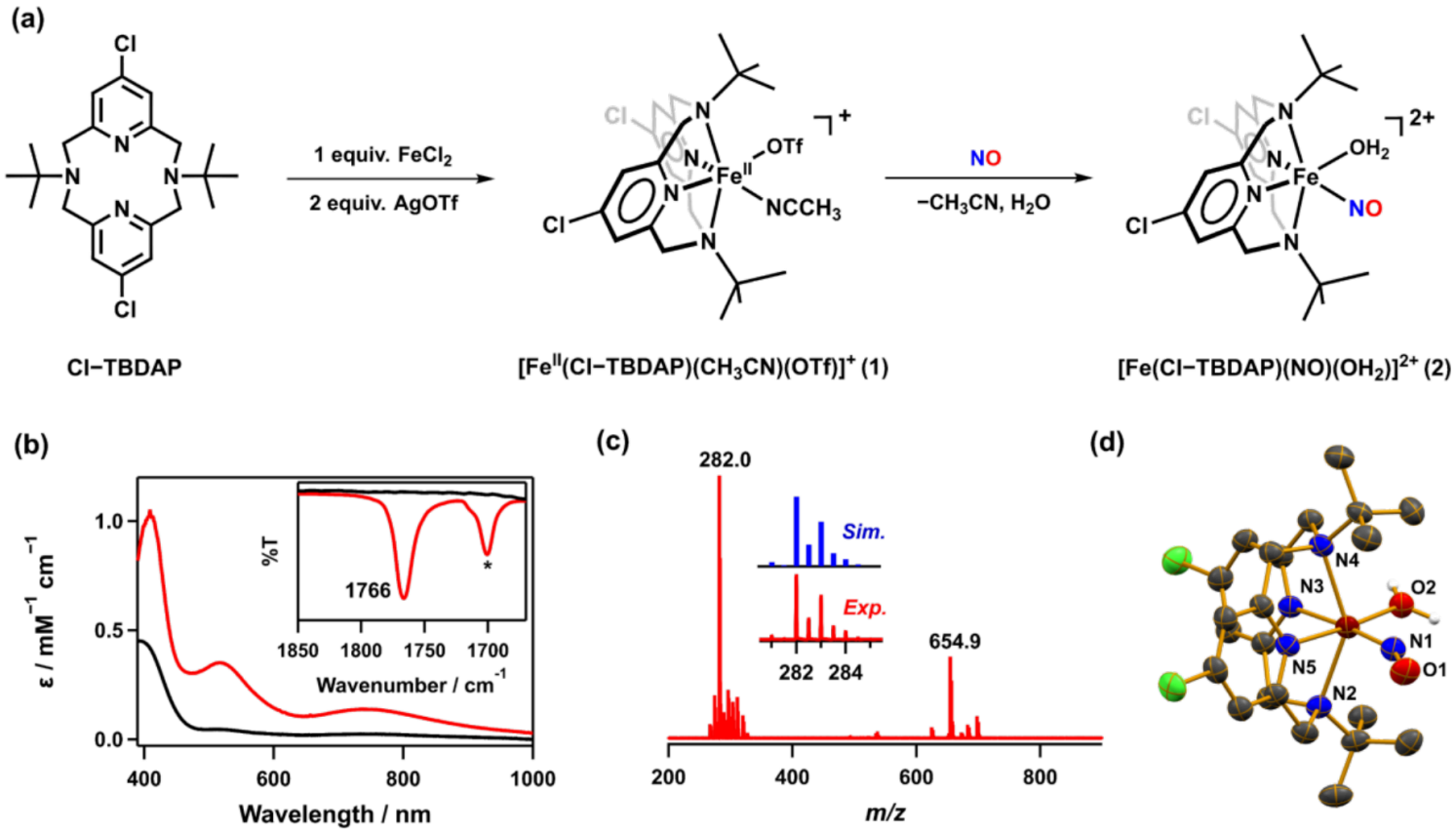


Figure 1

(a) Synthetic procedure of Fe precursor and nitrosyl complex (b) UV-vis absorption spectra of **1** (black) and **2** (red) in acetone at −40 °C. The inset shows FTIR spectra of **1** (black) and **2** (red). Asterisk (*) marks the C−O vibration due to an acetone molecule in the crystal. (c) CSI-MS spectrum of **2** in acetone at −30 °C. The peaks at *m/z* 282.0 and 654.9 correspond to $[Fe(Cl–TBDAP)(NO)(CH_3COCH_3)]^{2+}$ and $[Fe(Cl–TBDAP)(NO)(OTf)]^{+}$, respectively. The inset shows the simulated (blue) and experimental (red) isotope distribution patterns for the peak at *m/z* = 282.0. (d) ORTEP diagram of **2** with the thermal ellipsoids drawn at the 30% probability. Hydrogen atoms are omitted for clarity, except for the hydrogens of water. Fe, scarlet; O, red; N, blue; C, dark gray; Cl, green; H, white. Selected bond lengths (Å) and angle (°): Fe–N1 1.762(4), Fe–N2 2.307(4), Fe–N3 2.067(4), Fe–N4 2.309(4), Fe–N5 2.043(4), Fe–O2 2.062(3), N1–O1 1.157(4), and Fe–N1–O1 152.8(3).

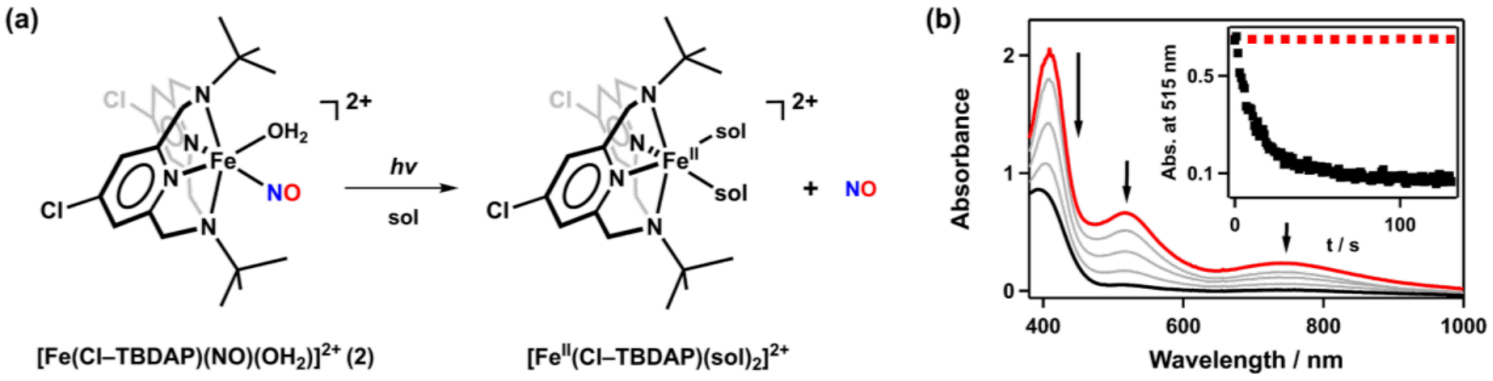


Figure 2

(a) Photolysis reaction of **2** upon irradiation with white light (λ_{irr} = 385–740 nm, 500 mW, xenon lamp) (b) UV-vis spectral changes of **2** (2.0 mM) upon irradiation in acetone at −40 °C. The inset shows the time courses of the absorption band at 515 nm in the presence (black) and absence (red) of light.

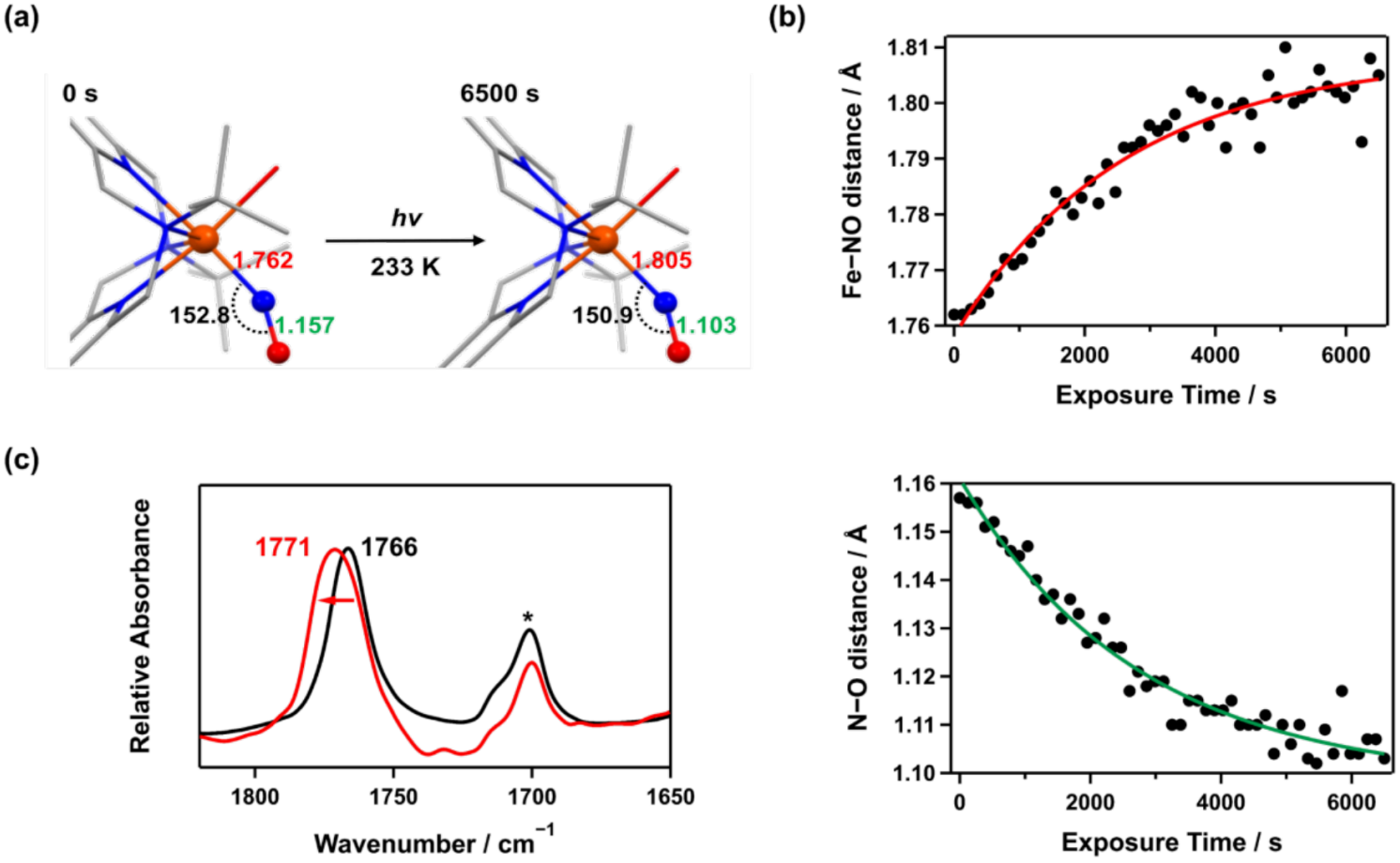


Figure 3

(a) Crystallographic description of the photoactivation of **2** at 233 K. (b) Time courses of Fe–NO (upper) and N–O (lower) bond length changes against irradiation time. The data points were collected every 130 seconds. (c) ATR-IR band shift of **2** after irradiation. The IR band of the N–O bond shifts from 1766 cm^{-1} (black) to 1771 cm^{-1} (red). Asterisk (*) marks the C–O vibration due to an acetone molecule in the crystal.

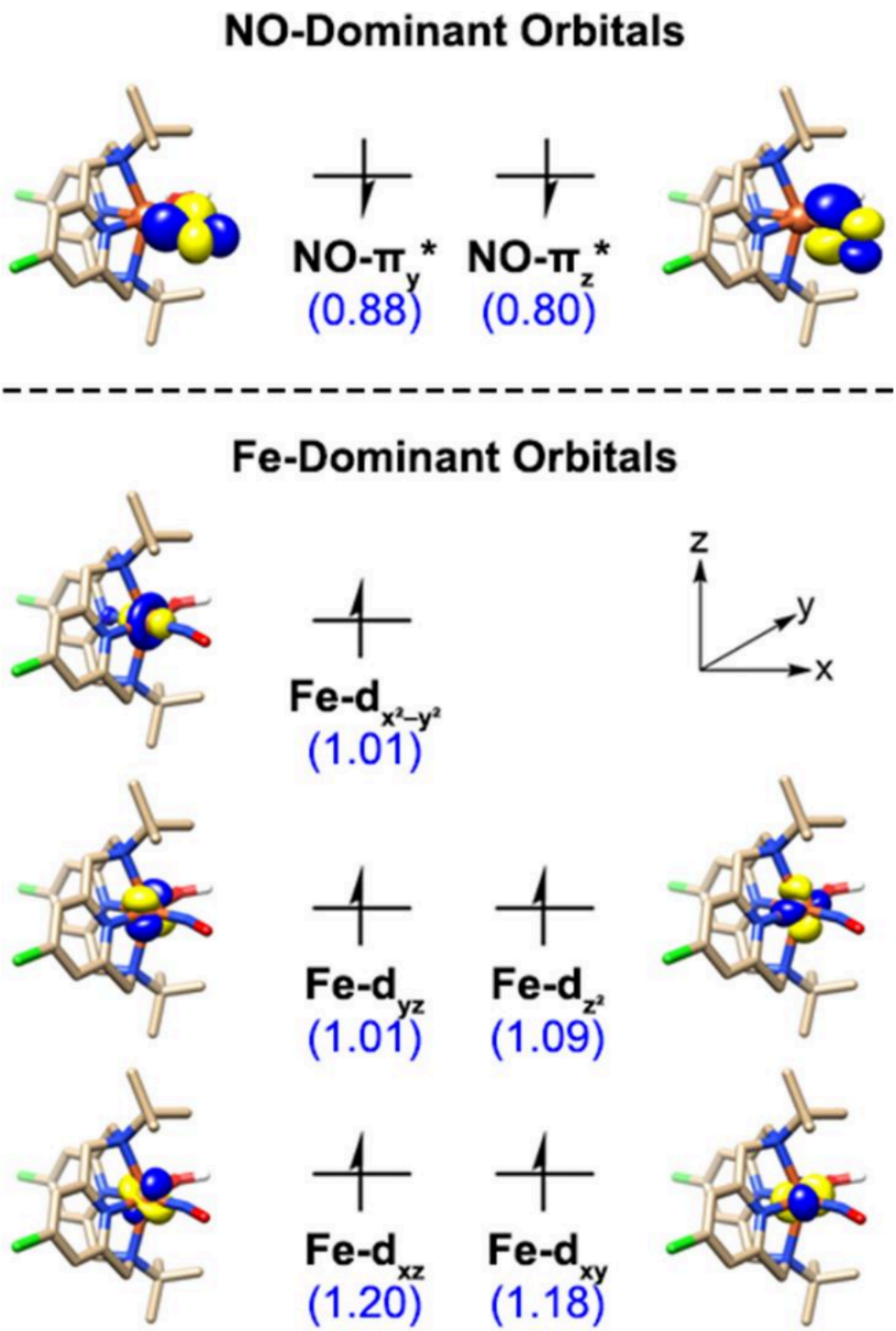


Figure 4

Ground-state electronic structure of **2** computed at the CASSCF(11,9)/def2-TZVP level of theory with a single root. The CAS wavefunction is projected into the Foster-Boys localized orbital manifold for visualization. Non-essential hydrogen atoms are omitted for clarity, and an isodensity value of 0.05 e/Å^3 is used for the orbital plots. Average occupation numbers are given in blue.

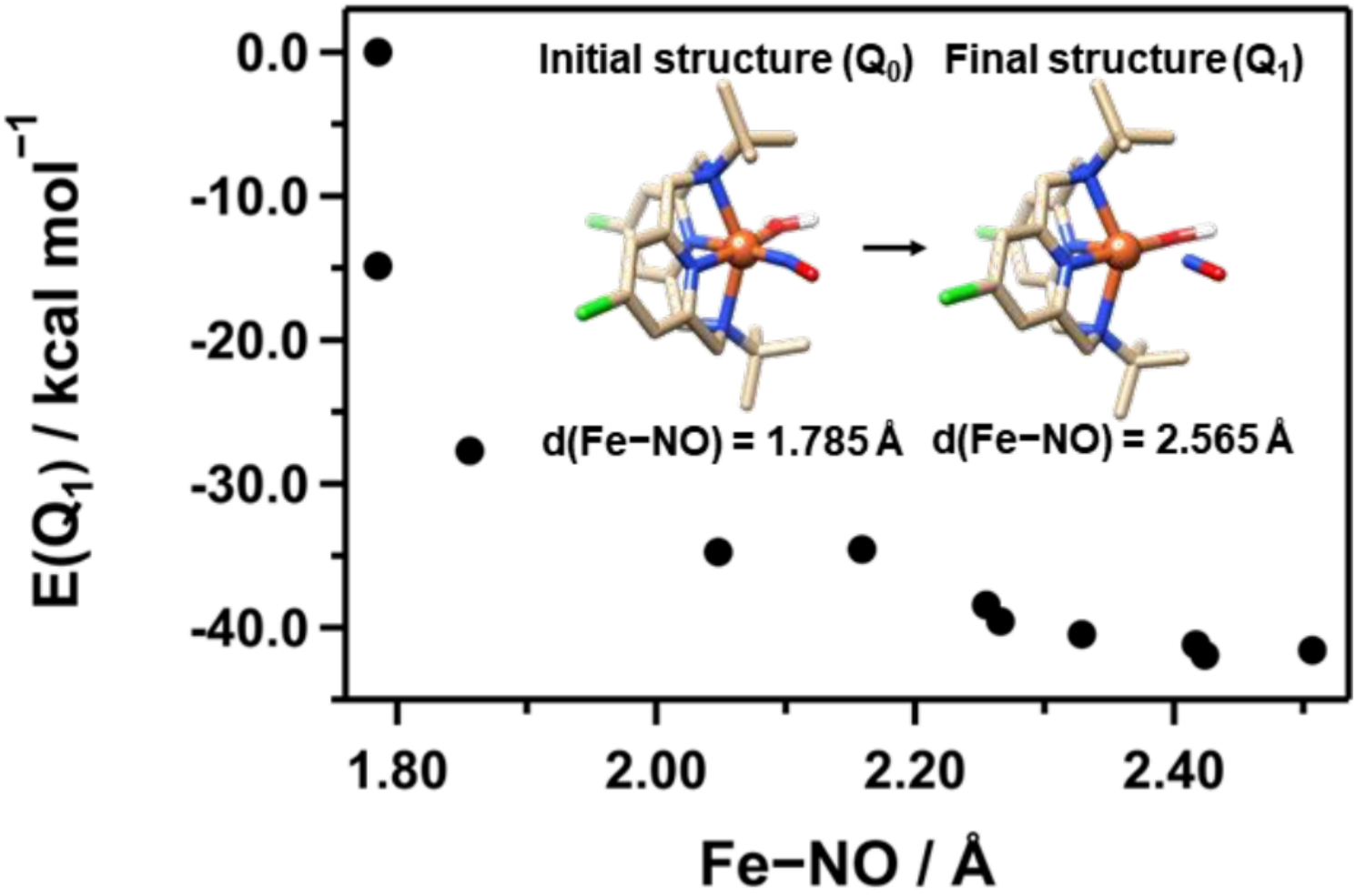


Figure 5

To confirm that the Q_1 state induces photolability, geometry optimization of the Q_1 state was performed using CASSCF(11,9)/SVP level of theory with 10 roots. During the optimization process, the energy of the Q_1 state decreased as the Fe–NO bond elongated. As a result, the Fe–NO complex dissociates into two separate molecules.

Supplementary Files

This is a list of supplementary files associated with this preprint. Click to download.

- SI.pdf
- GA.png